Multiobjective aerodynamic optimization of a microscale ducted wind turbine using a genetic algorithm

Emre ALPMAN*

Department of Mechanical Engineering, Faculty of Engineering, Marmara University, İstanbul, Turkey

Abstract: A two-objective aerodynamic optimization of a microscale ducted wind turbine was performed using a genetic algorithm. Two different fitness function pairs were considered for this purpose. In the first alternative the algorithm maximized the power produced while minimizing the drag force at a given wind speed and tip speed ratio. In the second alternative, however, the annual energy production was maximized while minimizing the maximum drag force developed between the cut-in and cut-off wind speeds. Computational fluid dynamics solutions performed for selected best designs showed that optimizations performed using the second alternative yielded better turbines, which could produce more power at lower drag. The best design of the second alternative was also observed to operate efficiently at a larger tip speed ratio range compared to the second alternative.

Key words: Ducted wind turbine, multiobjective optimization, genetic algorithm, computational fluid dynamics

1. Introduction

Wind turbines mounted in urban environments produce energy where it is needed and therefore eliminate the energy transportation problem [1–3]. Due to the lack of available space for large wind turbines in urban areas, emphasis is placed on small or micro wind turbines in these regions [1–4]. In addition to this, wind turbines in urban environments also typically operate at low wind speed conditions. Therefore, it is of great importance to increase the power output of such wind turbines [5]. By placing the rotor inside a duct the mass flow rate through the rotor can be successfully increased [5–21]. Since downstream of the rotor the geometry of the duct has basically a diffuser shape, ducted wind turbines are usually called diffuser augmented wind turbines (DAWTs) in the literature. The shape of the diffuser was shown to affect the performance of a DAWT [5]. Straight-walled diffusers [5,10,14,17] have simple geometry; however, a very long diffuser may be required for an effective increase in the mass flow rate [10,14]. The length of the diffuser can be decreased by placing a flange at the exit of the diffuser [5,10,14,18]. In [14], it was also shown that a diffuser with a curved inner wall performs better than a straight-walled one. The work in [15] included the optimization of the inner wall of the shroud of a DAWT by handling the problem simply as an internal flow problem. However, since the flow over the outer surface of the shroud is also important to increase the mass flow rate through the turbine (see the flanged diffuser designs in [5,10,14,18]), it was recommended in [8] and [20] that geometry optimization problems should be handled as external flow problems. Alternatively, ducts with airfoil-shaped cross-sections also increase the mass flow rate through the rotor by the circulation related to the lift force on the duct cross-section [5,6,20].

---

*Correspondence: emre.alpman@marmara.edu.tr

This radial lift force developing on the duct additionally leads to a larger wake expansion downstream of the turbine [5,6,22].

Increasing the flow velocity through the duct of a DAWT also increases the drag force developing on the blades. This leads to an increase in the flow resistance and consequently to a decrease in the mass flow rate [5,6,13]. Therefore, an optimum number of blades should be determined for effective power production from a DAWT [13]. In addition to the number of the blades, the blade geometry also affects the performance of a DAWT [16]. The blades of a horizontal augmented wind turbine are typically designed or optimized for a uniform oncoming wind [23–28]. However, the presence of the duct may considerably alter the flow entering the rotor plane and the blades may need to be redesigned for DAWTs [20].

In many studies, optimization of DAWTs was performed for maximum power production [9,11,15,18,20]. However, a DAWT design may have disadvantages like increased drag, weight, and cost [8,21]. Therefore, multiobjective optimization, which would try to maximize power production while minimizing the drag force, would be beneficial for DAWT designs [21].

This study contains a two-objective optimization of a microscale DAWT for maximum energy production at a minimum drag force on the turbine (rotor + duct). Diameter of the rotor was set to be 1 m. The elitist nondominated sorting genetic algorithm (NSGA-II) [29] was used for optimizations. According to [29], some of the classical optimization methods convert the multiobjective optimization problem into a single objective optimization problem in order to find a single optimum solution from the Pareto front. This not only requires a carefully weighted combination of the objectives but also the method should be applied many times to find different alternative solutions [30]. However, NSGA-II does not follow this conversion procedure; rather, it aims to find the Pareto front in a single run by using a fast nondominated sorting algorithm [29]. In the algorithms, once the offsprings are produced, the new generation is constructed from the parent and offspring population according to the nondomination rank and crowding distance of each individual. For details please refer to [29].

The fitness functions (drag force and power produced) were calculated using the ducted fan design code DFDC (http://web.mit.edu/drela/Public/web/dfdc/). Here, DFDC was selected mainly because of its ability to produce quick performance estimates for the DAWT geometries. The optimization process searches for Pareto optimal solutions for duct and blade geometries, number of blades, and longitudinal location of the rotor plane inside the duct. The duct has an airfoil-shaped cross-section consisting of a camber line represented using a cubic Bezier curve along with the thickness distribution of NACA 4-digit airfoils. The blade geometry was defined using spanwise distributions of twist angle and chord length, which were also both represented by cubic Bezier curves. The blades had NREL's S833 airfoil section along their span, and the clearance between the blade tips and the duct was set to be 2% of the blade radius.

In order to visualize the flow details around the optimized geometries, computational fluid dynamics (CFD) solutions were performed for some selected geometries using the open-source CFD software OpenFOAM. Here, at different tip speed ratios, power and drag coefficients, velocity, and pressure fields were predicted and presented.

2. Methodology

For two-objective optimizations using the NSGA-II algorithm a MATLAB code originally developed by Aravind Seshadri (shared at https://www.mathworks.com) was modified to interact with DFDC for fitness function evaluations. For a population composed of 40 individuals, optimizations were performed for 300 generations.

Two different cases that employ different fitness function pairs were considered. In Case I, the code sought to maximize power produced while minimizing the drag force at a specified wind speed. Since wind turbines are typically optimized for a given wind site [26,27], the Gökçeada region in Turkey was selected in this study for this purpose. The power and drag force calculations were performed at 6 m/s wind speed, which is the most probable wind speed in the selected region [26,27]. In Case II the power production was replaced by annual energy production (AEP), which was calculated as described in [30] using the Weibull parameters for the Gökçeada region in Turkey [26]. During the computations the cut-in and cut-off speeds were taken as 3 m/s and 15 m/s, respectively. The drag force in this second case was actually the maximum drag force obtained between these cut-in and cut-off speeds. Optimization studies were performed at a constant rotor rpm. Figure 1 shows the final Pareto fronts obtained at 250, 300, and 350 rpm for Case I. In this figure, power and drag force are normalized by their maximum values. According to this figure, the predicted Pareto fronts are nearly on top each other when the normalized objective function values are both less than 0.4. Therefore, the rest of the optimizations were performed at a rotation rate of 300 rpm.
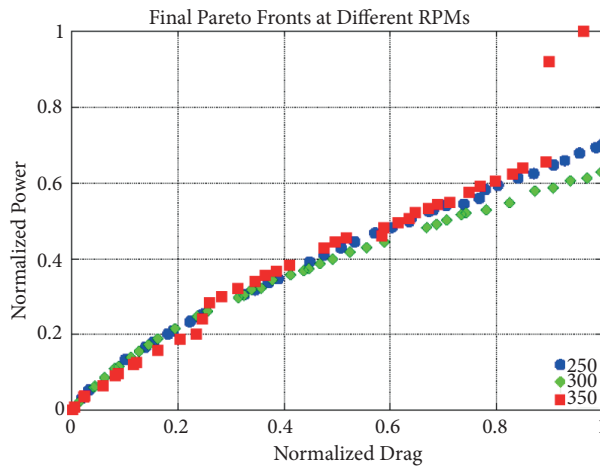
Figure 1. Final Pareto fronts at different rotor rpm values (Case I, V = 6 m/s).

The camber line of the airfoil-shaped cross-section of the duct was represented using a cubic Bezier curve, which is defined using four control points. In this study, the first control point was fixed at the leading edge of the profile and its position did not change. The second and third control points were axially positioned between 10% and 50% and between 50% and 90% of the chord length, respectively. The fourth one was fixed at the trailing edge. These last three control points were also allowed to move in the radial direction. The length of the duct and the maximum thickness of the profile were also specified as design parameters. In order to control the ratio of the duct exit area to the rotor area, the generated profile was also allowed to rotate about a point on its camber line, which axially coincided with the location of the rotor. The angle of this rotation was not allowed to exceed $10°$. As a result, the geometry of the duct was defined using eight design parameters.

For the geometry of the rotor blades, the spanwise twist angle and chord length distributions were defined using cubic Bezier curves. Here, the first and the fourth control points were located at the hub and the tip of the blade while the second and the third control point were allowed to move between the hub and the half span and between the half span and the tip, respectively. Although the same approach was used for twist angle and chord length, their internal control points were located separately. At each control point a representative twist angle or chord length was specified as a design parameter. As a result, the blade geometry was defined using a

total of 12 design parameters. The blades had the S833 airfoil profile and the twisting procedure was performed for about 30% chord of each airfoil section. The blades had zero lean angles.

Finally, the number of blades, which varied between 2 and 8, was added as the last design parameter. Hence, the optimization problem consisted of 21 design parameters.

The optimization code, which is based on the elitist NSGA-II algorithm, employs tournament selection with a mating pool size of half the population and a tournament size of two. The code produces offspring using simulated binary cross-over and polynomial mutations, with probabilities of 0.9 and 0.1, respectively. For fitness function evaluations the optimization code invokes the DFDC software and receives power and drag force predictions. After the fitness values are received for all the individuals, the optimization code continues with the genetic operators to produce the next generation.

In order to obtain the flow details around an optimized geometry, CFD solutions were performed using OpenFOAM. While any point on the Pareto front can be selected as an optimum solution, in this study the "best" solution was considered to be the one closest to the point (0,1) in the normalized power (AEP in Case II) vs. the normalized drag graph. This is equivalent to assuming that both objectives have the same importance for the design. For the CFD solutions the corresponding rotor and duct geometries were constructed using open-source FreeCAD and Gmsh software, respectively. Then an unstructured mesh was constructed around them using Gmsh. The final grid, consisting of more than 4 million cells, was composed of an inner region surrounding the rotor and an outer region surrounding the inner region. During the grid generation the inlet of the flow domain was located at three rotor diameters upstream while the exit of the flow domain was located at seven rotor diameters downstream of the turbine. The cylindrical outer boundary was located at four rotor diameters away from the axis of rotation. Flow velocity and exit pressure were specified at the inflow and outflow boundaries, respectively, while flow variables were set to their freestream values at the outer boundaries. Turbulence intensity and ratio of eddy viscosity to molecular viscosity were set to 1% and 0.1, respectively, at the inflow boundary. Finally, a no-slip boundary condition was applied at solid boundaries. Since the constructed mesh was not fine enough to resolve the boundary layer near the solid surfaces, wall functions were used for the turbulence quantities. Numerical solutions were obtained using the multiple rotating reference frame solver MRFSimpleFoam of OpenFOAM along with the realizable $k - \varepsilon$ turbulence model [31]. Here, the inner region was set to rotate with rotor speed while the outer region was kept stationary.

3. Results

3.1. Optimization results for Case I

In Case I the optimization process maximizes the power produced at a wind speed of 6 m/s while minimizing the total drag force on the duct and the rotor. Figure 2a contains the Pareto front of the initial population along with the Pareto fronts obtained at the 100th, 200th, and 300th generations. Initially only eight of the 40 individuals were nondominated; however, all of the individuals resided on the Pareto front in the other generations displayed in the figure. The figure also shows that there is very little improvement between the 200th and 300th generations, which indicates that the optimization algorithm converged. Figure 2b contains the Pareto fronts of the last ten generations (the last generation is represented with blue dots) along with the best individual, which is marked with a black dot. In order to compare the performance of the NSGA-II algorithm with other optimization methods, the problem was also solved using the PESA II [32] and MOEA/D [33] algorithms by using the same number of fitness function evaluations. PESA II employs a regional selection technique rather than the individual-based one of NSGA-II. On the other hand, MOEA/D decomposes the

problem into single-objective optimization problems associated with each individual in the population. These basic differences between the algorithms were the main reason for their selection. The final Pareto fronts yielded by PESA II and MOEA/D are included in Figure 2b as green triangles and red squares, respectively. Here, no parameter tuning was applied for any of the methods and the suggested values were used. According to the figure MOEA/D did not perform well for this problem. Although some of the optimum solutions of PESA II dominated those of NSGA-II, the diversity of the former's Pareto front is not as good as the latter's. Also, none of the PESA II optimum solutions were able to dominate the suggested "best" solution of NSGA-II. Therefore, NSGA-II was continued to be used for the rest of the studies.
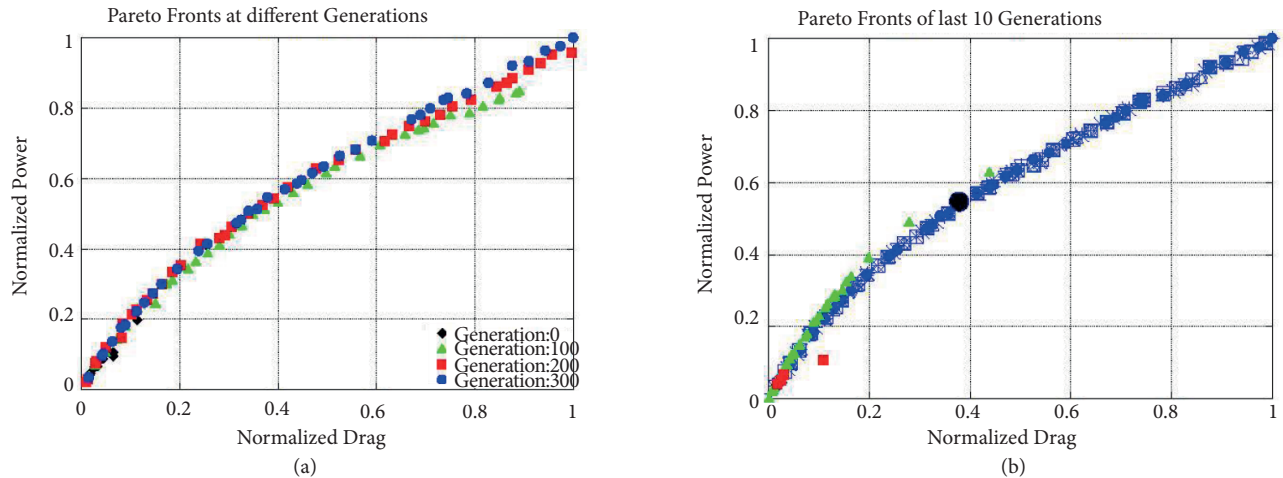
Figure 2. Pareto fronts at (a) different generations, (b) last ten generations and final Pareto fronts by PESA II (green triangles) and MOEA/D (red squares) (Case I).

The cross-section of the best individual and a detailed view of its rotor blades are displayed in Figure 3 The longitudinal location of the rotor along the duct axis was found to be at the throat of the duct.

Figure 4a shows the power coefficient (Cp) versus the tip speed ratio (λ) curve for the best design obtained at 6 m/s wind speed (designated as ducted in the figure). Predictions were obtained at 100, 200, 300, and 400 rpm where the corresponding tip speed ratios were 0.8727, 1.745, 2.618, and 3.491, respectively. The figure also contains the Cp vs. λ curve of the bare rotor of the best design (designated as unducted). For both curves the Cp was calculated using freestream dynamic pressure and the rotor area. It is clear from this figure that the presence of the duct clearly increases the amount of power produced as well as the range of tip speed ratios the turbine could operate. As expected, the maximum Cp of the ducted case was achieved at 300 rpm, at which the geometry of the turbine was optimized. At this rotation rate the bare rotor did not even produce positive torque. The best Cp value predicted for the bare rotor was almost 1/3 of the Cp of the ducted rotor at the same rotor speed. While the presence of the duct successfully increased the power production, it also increased the frontal projected area of the turbine. Therefore, the Cp of the ducted rotor was recalculated using the duct exit area rather than the rotor area, and the result is displayed in Figure 4a as ducted2. Since the duct exit area was more than four times larger than the rotor area, the efficiency of the ducted rotor fell below the bare one at 100 and 200 rpm.

The effects of the duct on the drag force are displayed in Figure 4b, which contains the drag coefficient of the rotor for ducted and bare rotors along with the drag coefficient of the whole turbine. It is clear that the duct increased the drag force on the rotor due to mass flow augmentation (typically called rotor thrust in
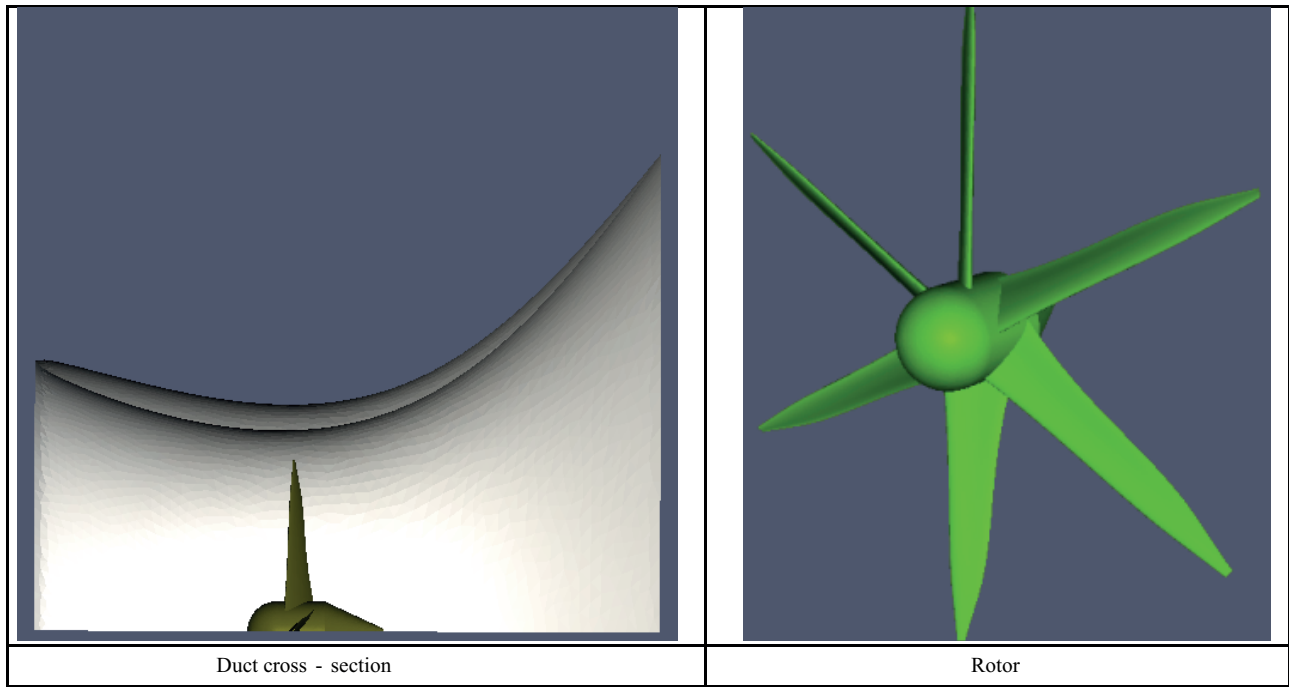
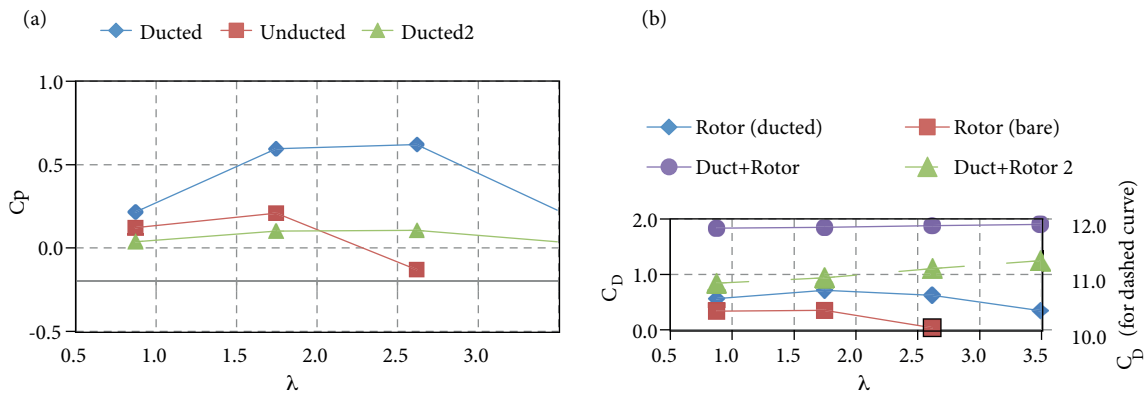**Figure 3**. Optimized turbine geometry (Case I).

**Figure 4**. (a) Cp vs. λ (b) CD vs. λ curves for the best design (Case I).

wind turbine terminology [34]). Since drag coefficients of blunt bodies are typically calculated using the frontal projected area of the body, duct exit area was used to calculate the C_D of the whole turbine (duct+rotor) while rotor area was used for calculating the C_D of the rotor. In order to better see the impact of the duct on the drag force, the drag coefficient of the turbine was calculated using rotor area as displayed using a dashed line and a secondary vertical axis in Figure 4b. The values on the secondary vertical axis clearly indicate that even though the duct augments the power production and the operating tip speed ratio range, its impact on the drag force is much more severe.

Figure 5 shows the contours of axial velocity on a radial plane cutting a rotor blade. In the figure velocity is displayed in meters per second. The duct clearly accelerated the flow through the rotor disk, especially at the tip region of the blade. Compared to the bare rotor, the wake of the center body of the ducted turbine was much

larger. This was mainly because the fluid elements were drawn toward the duct surface due to the Coanda effect [35]. This phenomenon not only increased the circulation around the duct cross-section but also enhanced the wake expansion, which is an important factor for effective power generation [20]. The corresponding pressure coefficient distributions are displayed in Figure 6. According to this figure the duct effectively increases the pressure difference across the rotor. The low-pressure region near the duct surface downstream of the rotor helped reduce flow separation on the inner surface of the duct. However, this low-pressure region in the inner surface along with the high-pressure region on the outer surface of the duct increased the drag force considerably.


| (a) | (b) |
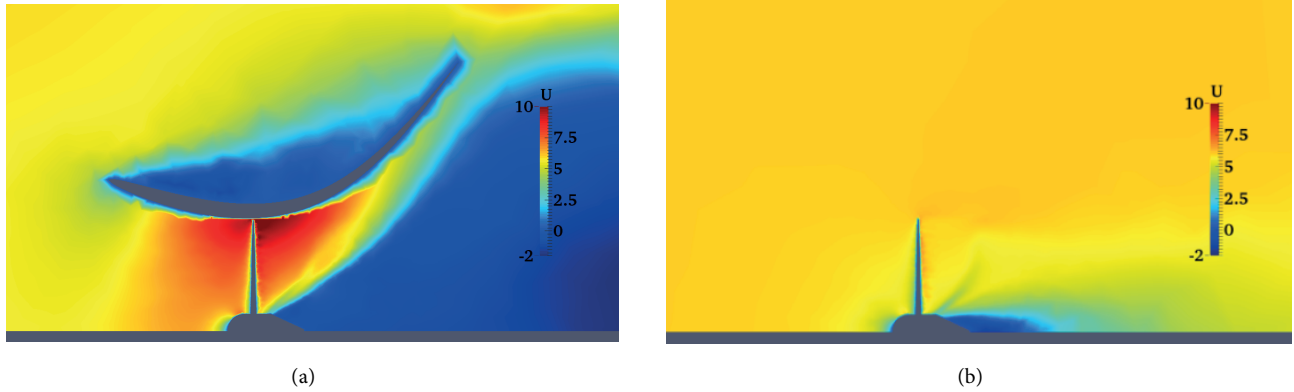
Figure 5. Axial velocity contours (in m/s) for (a) ducted, (b) bare rotor (Case I).

| (a) | (b) |
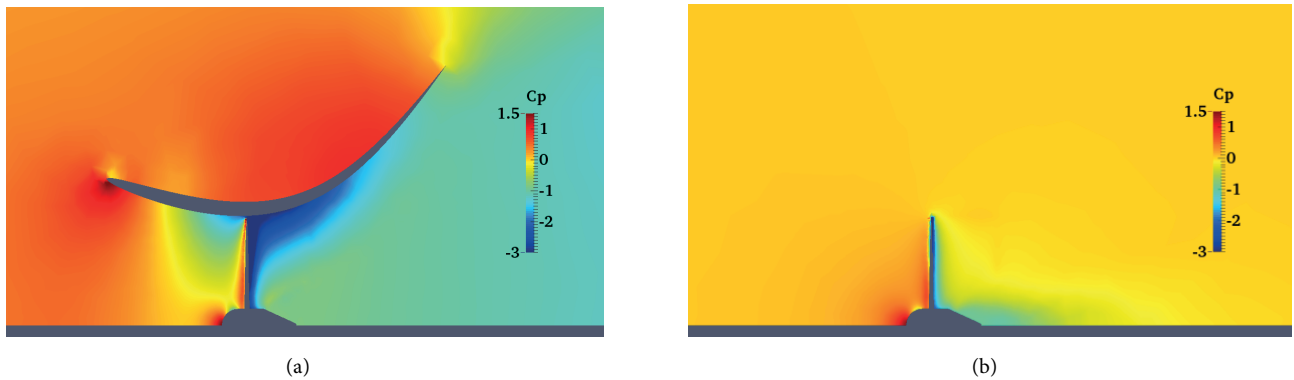
Figure 6. Pressure coefficient contours for (a) ducted, (b) bare rotor (Case I).

3.2. Optimization results for Case II

In Case II the optimization process maximizes the AEP while minimizing the maximum drag force developing on the duct and the rotor. The AEP was calculated between cut-in and cut-off wind speeds of 3 m/s and 15 m/s, respectively, with a 1 m/s increment. Figure 7a contains the Pareto front of the initial population along with the Pareto fronts obtained at the 100th, 200th, and 300th generations. Except for the initial generation, all of the individuals resided on the Pareto fronts of the corresponding generations. Very little improvement was observed between the 200th and 300th generations, which again indicates the convergence of the algorithm. Figure 7b contains the Pareto fronts of the last ten generations (the last generation is represented with blue dots) along with the best individual, which is marked with a black dot. Here, the best individual was selected in the same manner as in Case I.
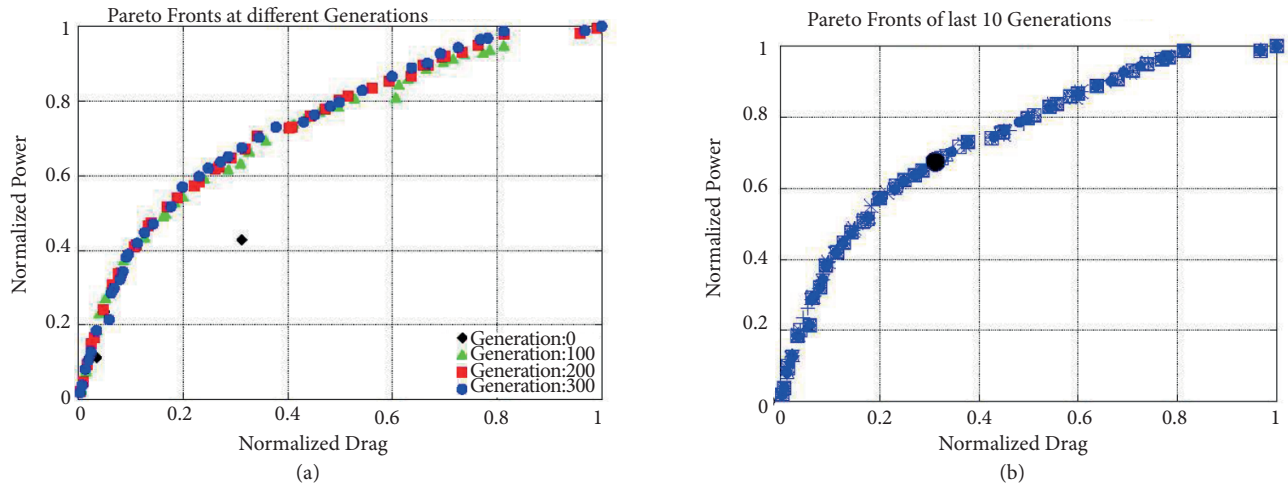
Figure 7. Pareto fronts at (a) different generations, (b) last ten generations (Case II).

The resulting geometry of the best individual along with a detailed view of the rotor blades are displayed in Figure 8. The duct design in this figure turned out to be shorter and less cambered compared to the one displayed in Figure 3. In addition to this, the rotor plane is located slightly downstream of the duct throat.
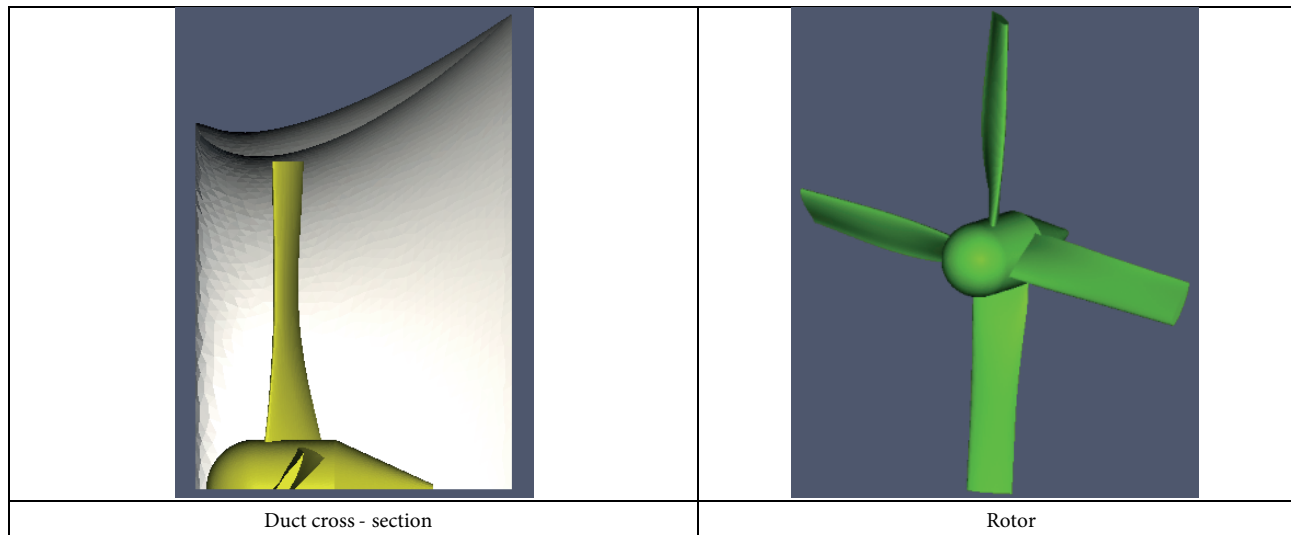

Figure 8. Optimized turbine geometry (Case II).

Moreover, the optimizations of Case II yielded four-bladed rotors in contrast to the six-bladed designs of Case I. Compared to their counterparts in Figure 3, the blades shown in Figure 8 were less tapered but more twisted, especially at the root region.

In order to compare the power predictions for the best designs of Cases I and II, the ratio of the Cp values of Case II's best design over Case I's best design was calculated and is presented in Figure 9a. In this figure the blue curve represents the Cp values calculated using the rotor area (which is constant for both cases) and the red curve represents the Cp values calculated using the duct exit area. According to the blue curve, the best design of Case II produces more power at higher rpm (or λ) values, especially at 400 rpm ($\lambda = 3.491$),

where the Cp ratio is more than 3.3. On the other hand, the best design of Case I was predicted to produce more power at lower tip speed ratios. However, the red curve clearly shows that the efficiency of the best design of Case II is much higher than that of Case I at all tip speed ratios.
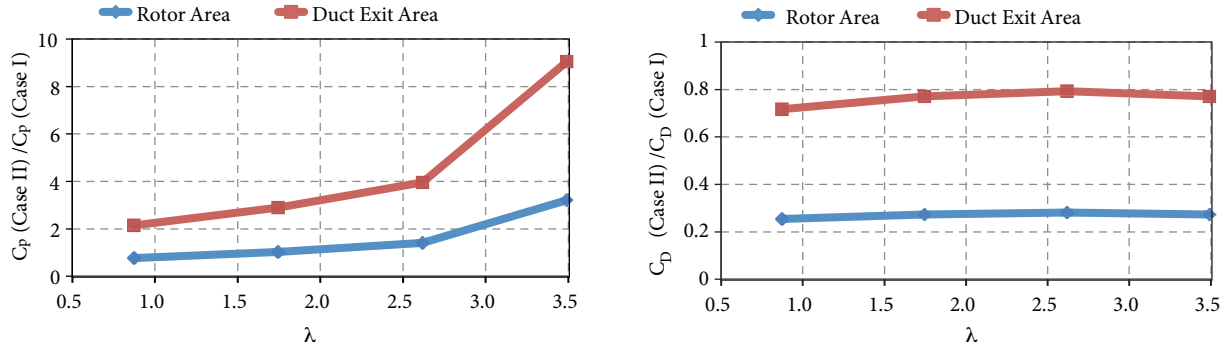
Figure 9. (a) Cp, (b) CD ratio (Case II / Case I) vs. λ curves.

In order to compare the drag loading on the turbines, the ratios of the total drag coefficients of the best designs of Cases II and I are displayed in Figure 9b. Once again the blue curve represents the ratio of the coefficients calculated using the rotor area while the red curve is for the coefficients calculated using the duct exit area. It is clear from this figure that the best design of Case I experiences more than 3.5 times more drag force while it produces less power. This situation becomes more severe when the frontal projected areas of the geometries are used in the calculations.

The contours of axial velocity on a radial plane cutting a rotor blade for ducted and bare rotor at 6 m/s wind speed and 200 rpm are shown in Figure 10. Again the velocity is represented in meters per second. Even though acceleration of flow through the rotor disk is evident from this figure, it is not as high as that observed for Case I in Figure 5. Also, the low-speed region observed in the vicinity of the trailing edge of the duct in Figure 10 indicates flow separation at this region. Such a flow separation was not observed in Figure 5 although, downstream of the rotor, the duct cross-section of the best design of Case I is much steeper than that of Case II. This situation can be explained considering the pressure distributions displayed in Figure 11. According to this figure, although the pressure drop across the rotor is higher for Case II compared to Case I, the low-pressure region in the vicinity of the duct surface does not extend far downstream toward the trailing edge of the duct. Hence, the duct of the Case II design did not take advantage of the Coanda effect as much as the duct of the Case I design did.
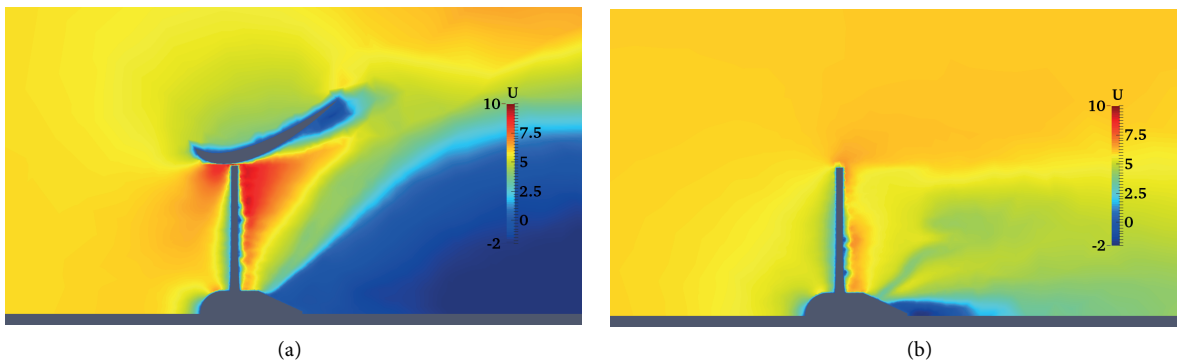
Figure 10. Axial velocity contours (in m/s) for (a) ducted, (b) bare rotor (Case II).
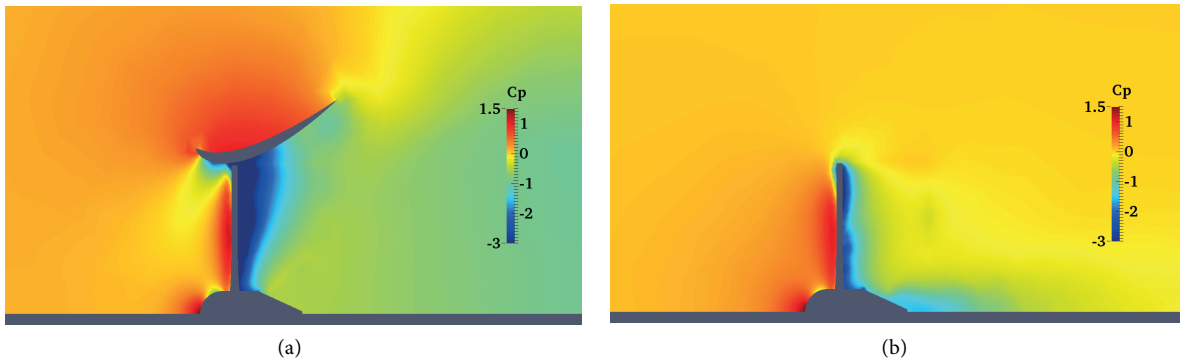
626

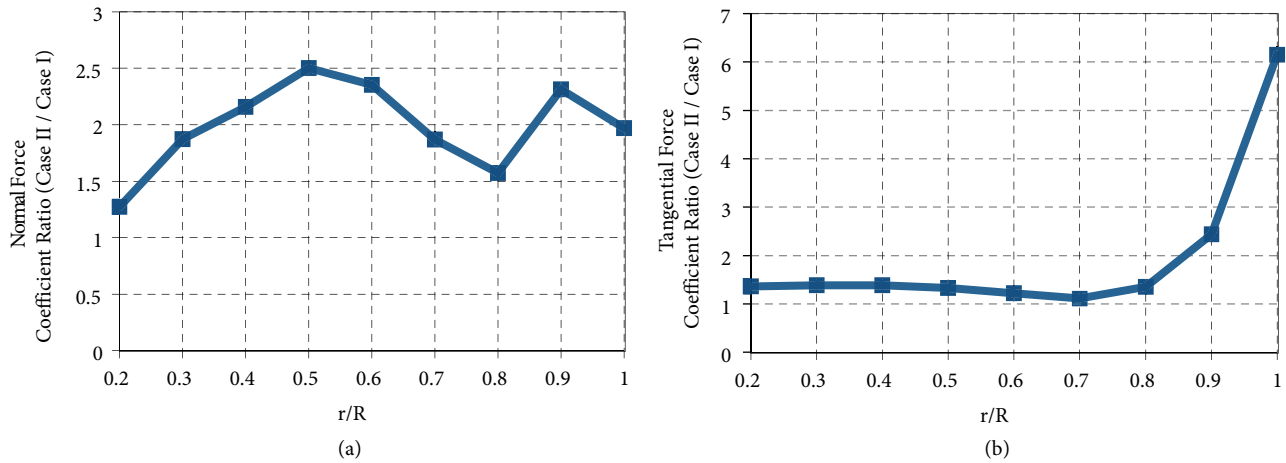Figure 11. Pressure coefficient contours for (a) ducted, (b) bare rotor (Case II).

Figure 12. Sectional force ratios at 200 rpm (Case II / Case I).

4. Conclusions

The following conclusions could be drawn by examining the CFD results:

- The duct not only augments the power production of the turbine but also enlarges the tip speed ratio range where the rotor could produce positive torque. However, the drag force on the turbine would also considerably increase.

- Pressure drop across the rotor would delay flow separation on the duct surface that would normally occur without the rotor. Therefore, the effect of the rotor must be included during the design optimization of the duct of a DAWT.

- The power coefficients of the ducted turbines exceeded the Betz limit when rotor area was used in the calculation of this coefficient. However, this did not happen when the duct exit area was used instead of the rotor area.

- Maximizing AEP for a range of wind speeds (Case II) instead of maximizing power generated at a selected wind speed (Case I) yielded better turbine designs, which produced higher power while experiencing lower drag force.

- Despite the higher flow rate augmentation of the Case I design, the Case II design produced more power due to its rotor blade design. This clearly showed that the geometry of the duct and the rotor blades should be optimized jointly.

Design optimization studies for DAWTs observed in the literature mainly focused on optimizing either the duct geometry or the blade geometry. To the author's best knowledge this is the first study that aims to optimize the rotor and duct geometries simultaneously. In addition to this, the effect of using power produced or AEP as one of the objectives was also investigated. The author's having not come across such a study previously was the main motivation behind this paper.

Acknowledgment

References

[1] Kaldellis J, Zafirakis D, Kondili E, Papapostolou C. Trends, prospects and R&D directions of the global wind energy sector. In: EWEA 2012 Annual Event; 16–19 April 2012; Copenhagen, Denmark. pp. 1403-1411.

[2] Mertens S. Wind energy in the built environment: concentrator effects of buildings. PhD, Delft University of Technology, Delft, the Netherlands, 2006.

[3] Cace J, ter Horst RE, Syngellakis HK, Power IT. Urban Wind Turbines. Guidelines for Small Wind Turbines in the Built Environment. Brussels, Belgium: Wineur Intelligent Energy Europe, 2007.

[4] Grant A, Johnstone C, Kelly N. Urban wind energy conversion: the potential of ducted turbines. Renew Energ 2008; 33: 1157-1163.

[5] Gomis LL. Effect of diffuser augmented micro wind turbines features on device performance. MSc, University of Wollongong, Wollongong, Australia, 2011.

[6] Hansen MOL, Sørensen NN, Flay RGJ. Effect of placing a diffuser around a wind turbine. Wind Energy 2000; 3: 207-213.

[7] Phillips DG, Flay RGJ, Nash TA. Aerodynamic analysis and monitoring of the Vortec 7 diffuser-augmented wind turbine. IPENZ Transactions 1999; 26: 13-19.

[8] Lawn CJ. Optimization of the power output from ducted turbines. P I Mech Eng A-J Pow 2003; 217: 107-117.

[9] Matsushima T, Takagi S, Muroyama S. Characteristics of a highly efficient propeller type small wind turbine with a diffuser. Renew Energ 2006; 31: 1343-1354.

[10] Ohya Y, Karasudani T, Sakurai A, Abe KI, Inoue M. Development of a shrouded wind turbine with a flanged diffuser. J Wind Eng Ind Aerod 2008; 96: 524-539.

[11] Hu SY, Cheng JH. Innovatory designs for ducted wind turbines. Renew Energ 2008; 33: 1491-1498.

[12] Wang F, Bai L, Fletcher J, Whiteford J, Cullen D. The methodology for aerodynamic study on a small domestic wind turbine with scoop. J Wind Eng Ind Aerod 2008; 96: 1-24.

[13] Wang SH, Chen SH. Blade number effect for a ducted wind turbine. J Mech Sci Technol 2008; 22: 1984-1992.

[14] Ohya Y, Karasudani T. A shrouded wind turbine generating high output power with wind-lens technology. Energies 2010; 3: 634-649.

[15] Foote T. Numerical modeling and optimization of power generation from shrouded wind turbines. MSc, Washington University, St. Louis, MO, USA, 2011.

[16] Shive M, Crawford C. Ducted turbine blade optimization using numerical simulation. In: The 21st International Offshore and Polar Engineering Conference; January 2011.

[17] Kosasih B, Tondelli A. Experimental study of shrouded micro-wind turbine. Procedia Eng 2012; 49: 92-98.

[18] Kannan TS, Mutasher SA, Lau YK. Design and flow velocity simulation of diffuser augmented wind turbine using CFD. Journal of Engineering Science and Technology 2013; 8: 372-384.

[19] Hjort S, Larsen H. A multi-element diffuser augmented wind turbine. Energies 2014; 7: 3256-3281.

[20] Aranake AC, Lakshminarayan VK, Duraisamy K. Computational analysis of shrouded wind turbine configurations using a 3-dimensional RANS solver. Renew Energ 2015; 75: 818-832

[21] Liu J, Song M, Chen K, Wu B, Zhang X. An optimization methodology for wind lens profile using computational fluid dynamics simulation. Energy 2016; 109: 602-611.

[22] Franković B, Vrsalović I. New high profitable wind turbines. Renew Energ 2001; 24: 491-499.

[23] Giguere P, Selig MS. Design of a Tapered and Twisted Blade for the NREL Combined Experiment Rotor. NREL/SR-500-26173. Golden, CO, USA: NREL, 1999.

[24] Eke GB, Onyewudiala JI. Optimization of wind turbine blades using genetic algorithm. Global Journal of Researches in Engineering 2010; 10: 22-26.

[25] Ceyhan O. Aerodynamic design and optimization of horizontal axis wind turbines by using BEM theory and genetic algorithm. MSc, Middle East Technical University, Ankara, Turkey, 2008.

[26] Sağol E. Site specific design optimization of a horizontal axis wind turbine based on minimum cost of energy. PhD, Middle East Technical University Ankara, Turkey, 2010.

[27] Alpman E, Kımıllı MO, Erişik A, Şahin E. Site-specific optimization of a small scale horizontal axis wind turbine via micro genetic algorithm. Isı Bilimi ve Tekniği Dergisi 2014; 34: 123-136.

[28] Alpman E. Effect of selection of design parameters on the optimization of a horizontal axis wind turbine via genetic algorithm. J Phys Conf Ser 2014; 524: 012044.

[29] Deb K, Pratap A, Agarwal S, Meyarivan TAMT. A fast and elitist multiobjective genetic algorithm: NSGA-II. IEEE T Evolut Comput 2002; 6: 182-197.

[30] Hansen MO. Aerodynamics of Wind Turbines. London, UK: Earthscan, 2015.

[31] Shih TH, Liou WW, Shabbir A, Yang, Z, Zhu J. A New K-Epsilon Eddy Viscosity Model for High Reynolds Number Turbulent Flows: Model Development and Validation. NASA Technical Memorandum 106721. Washington, DC, USA: NASA, 1994.

[32] Corne DW, Jerram NR, Knowles JD, Oates MJ. PESA-II: Region-based selection in evolutionary multiobjective optimization. In: 3rd Annual Conference on Genetic and Evolutionary Computation; 2001.

[33] Zhang Q, Li H. MOEA/D: A multiobjective evolutionary algorithm based on decomposition. IEEE T Evolut Comput 2007; 11: 712-731.

[34] Burton T, Sharpe D, Jenkins N, Bossanyi E. Wind Energy Handbook. New York, NY, USA: John Wiley & Sons, 2001.

[35] Hibbeler RC. Fluid Mechanics. New York, NY, USA: Pearson, 2015.